Disease Prognosis of Fetal Heart's Four-Chamber and Blood Vessels in Ultrasound Images Using CNN Incorporated VGG 16 and Enhanced DRNN

Someshwaran Gunasekaran
Department of Electronics and Communication Engineering
College of Engineering and Technology
SRM Institute of Science and Technology
Kattankulathur-603 203, Chengalpattu, Tamil Nadu, India
sg1922@srmist.edu.in

Sarada Vivekasaran
Department of Electronics and Communication Engineering
College of Engineering and Technology
SRM Institute of Science and Technology
Kattankulathur-603 203, Chengalpattu, Tamil Nadu, India
saradav@srmist.edu.in

Abstract: *Fetal Heart Disease (FHD) based Structural Heart Disorders (SHD) occur when certain features of the heart develop abnormally. These flaws may cause blood flow to circulate in the erroneous spot, slow down, or be utterly blocked. Heart Defects (HD) caused via FHD or disorders that primarily impact embryonic heart conditions are alternatively referred to as Congenital Heart Defects (CHD). Multiple prior investigation algorithms such as Multi-Resolution Convolutional Neural Network (MRCNN), Deep Convolutional Neural Network (DCNN), Faster-RCNN (FRCNN) and DANomaly Wgan-GP and Convolutional Neural Network (DGACNN) rendered in the detection of FHD. Yet, the models have endured several challenges due to fuzzy constraints and irrelevant adherence. The intended aim is to detect the dilemma of the fetal heart in UltraSound (US) images using two distinct tier methods. The initial tier detects the fetal heart chamber's walls and valves using the Convolutional Neural Network (CNN)-incorporated Visual Geometry Group 16 (VGG 16) technique for processing fetal ultrasound images, allowing it to detect and dissolve anomalies in heart walls. This initial investigation concerns improving the image's quality in each subsequent sequence, from lowest to most improved using the conventional Augmented Wiener Filtering (AWF) approach. Succeeding, an instance-level Region of Interest (ROI) segmentation for exploiting the feature mining approach will be carried out via spatial features masking and ground-truth labeling framework for septal defect diagnosis. The second tier determines the flaws in fetal heart blood flow size, structure and vessels utilizing Deep Recurrent Neural Network (DRNN) integrated with region-based texture characteristics Local-Binary-Pattern (LBP), Histogram-of-Oriented-Gradient (HOG) and the Bags Of Features (BOF) segmentation framework via image acquiring. In eventual, the histogram equalization enhancement algorithm with Median Modified Wiener Filter (MMWF) is enumerated to enhance the visual quality, tests for signal-to-noise ratio, rate of variations, and noise proportion for sorting the blood vessels of the input fetal image. The analyzed CNN's VGG 16 and DRNN model's efficiency via Matrix Laboratory (MATLAB) has detected the cardiac features both in normal and abnormal ranges with an overall accuracy of 99.89% and 98.7%.*

Keywords: *Fetal heart disease, ultrasound images, augmented wiener filter, median modified wiener filter, region of interest, convolutional neural network, visual geometry group 16, deep recurrent neural network.*

Received March 20, 2024; accepted October 14, 2024
https://doi.org/10.34028/iajit/21/6/13

1. Introduction

Fetal Heart Disease (FHD) is a serious congenital abnormality with an increase in annual prevalence of 6-8 percent [32]. Despite adept surgery, many infants may die within the first few weeks after birth from myocardial and pulmonary complications induced by severe cardiac pathologies. So, it's crucial to prevent and treat FHD in prior. Fetal intervention at the premature phase of pregnancy i.e., 2nd trimester (18 to 22 weeks) [42] will be more beneficial with encouraging results. With the subsequent prognosis outcomes, fetal therapy is intended to improve cardiac perfusion and minimize ischemia by restoring forward flow and lowering intraventricular pressures.

This paves the path to Fetal Echocardiography (FE) which has been a prominent screening method for early diagnosis of fetal cardiac malformations due to its reliability, sensitivity, non-invasive nature and real-time imaging [16, 23, 50]. Further, the prenatal ultrasound detection parts the crucial 4-Chamber Scan (4CS) and 3-Vessel Scan view (3VS) depicted in Figure 1, allowing for a full evaluation of fetal heart development [25, 56] which is acquired via ultrasound transducer by 90 degrees to the mid-sagittal part of the embryonic heart and fine-tuning the acquired image. However, the 4CS and 3VS captured by detached observers at different views result in diverse images, making the obstetrician a very challenging task to distinguish its size and location [22, 34, 47]. To alleviate this dispute, a computer-driven approach has gained prominence in enabling obstetricians to automatically locate the four chambers and blood vessels [17, 33]. This automated procedure assists in improving the efficiency of FHD diagnosis.

However, there still exists several flaws such as poor resolution and high speckles. Moreover, there is a high degree of similarity in discrimination between the four cardiac chambers and blood vessels.

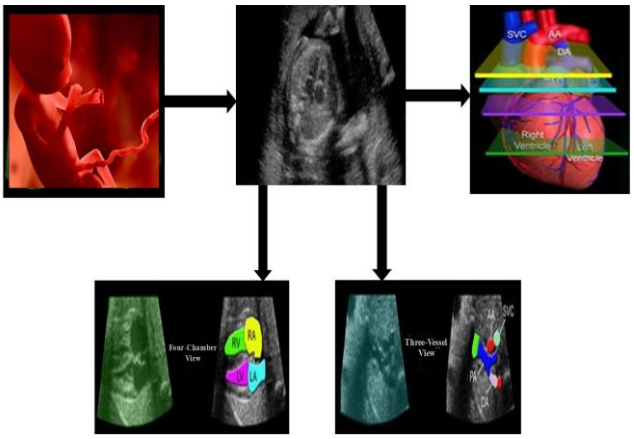

Figure 1. Fetal heart's ultrasound image for four-chamber and three-vessel view.

Considering these challenges, a meta-heuristic detection system is necessary to characterize the invariant-position, structure-specific, and spatial features of 4CV and 3VS. Machine Learning (ML) and Deep Learning (DL) are at the forefront of use in several medical domains for their learning invariant features which include screening breast cancer [11, 57], classifying tumor [41], clustering EEG signals and classification [7, 49], autism screening [51, 52] and brain disease diagnosis [36, 45]. At current, DL is more prevalent in heart ultrasound images to segment, classify and detect adult and fetal hearts [6, 8, 26, 31]. Convolutional Neural Network (CNN) and Recurrent Neural Network (RNN) are the foremost representative DL methods to learn and discriminate robust features from medical images [2, 4]. The inert features of congenital heart acquired via CNN necessitate the automatic aiding system in detecting FHD features accurately.

Recent findings reveal that CNN is more suited for detecting both fetal and adolescent patterns in ultrasound images where Selvathi and Chandralekha [39] propounded a novel acoustic Deep Convolutional Neural Network (DCNN) to predict ventricular endocardium in adolescent ultrasound images. The DCNN incorporated prior knowledge of the heart's scale and label for the automatic acquirement of the left heart's constraints prediction. Following the framework of DCNN, Smistad and Lovstakken [44] put forward an automatic DCNN framework for fetal heart vessel detection via ultrasound images from echocardiography recordings which integrates a so-called substantial random field technique in the prognosis of congenital heart. Xu *et al*. [55] implied a dilation-based convolution chain framework to enhance the field of image vision via the Gaussian filtering and extracted substantial fetal cardiac info. The CNN chain model features global and local data info from spatial maps to segment and prognose the ventricular elements in Fetal Cardiac (FC) regions precisely. In subsequent, a new deploying neural network Faster RCNN is propounded by Patra and Noble [33] to extract the fetus's fuzzy traits from the four-chamber and classify the spatial data to detect the embryo's 4CV anatomical features. Ensuing with the work of Faster-RCNN, Wu *et al*. [54] further deployed the FRCNN model to extract the fetal heart region from the FC image which subsequently combined with DGACNN to classify the extracted features of 4CV and 3VS. Eventually, Gong *et al*. [19] implied DANomaly Wgan-GP and CNN (DGACNN) for effective prognosis of FHD in US imaging via region-based extraction which permits high-scale accuracy with low latency in detection. Nurmaini *et al*. [30] developed an enhanced Mask-RCNN (MRCNN) for early detection and diagnosis of FHD which deployed the data analytical method of DL to diminish the necessity for expertise and vision error, leading to the prediction accuracy of upto 90%.

Succeeding the anatomical work of DL, a meta-heuristic implementation model named RNN is developed by Choi *et al*. [12] for early phase fetal detection i.e., 18 months screening of fetal heart dilemma and regulates the timely events of disease diagnosis. The efficiency of the model has been assessed with logistic regression in the parametric analysis. In subsequent, Narmadha *et al*. [29] further implied RNN utilizing the integrated models of Gated Recurrent Unit (GRU) and Long Short-Term Memory (LSTM) to forecast myocardial abnormalities. Leveraging the combination model and ROI segregation with accessible data, the GRU predicted the anomalies more accurately than the LSTM. Later on, Babu *et al*. [5] put forth a hybrid strategy for assessing multiple sorts of embryonic conditions by integrating Grey WolF optimization (GWF) in extracting the features with an auto-encoder-based RNN in disease detection which utilized multiple datasets including Cleveland, Mammographic, and Hungarian. The suggested model enumerated with a precise rate of 90.82% efficacy in detection. In advance, future enhancement can possibly be addressed via various combined tactics that attain more accuracy than current procedures. In closing, Shinde and Martinez-Ovando [48] enumerated the efficacy of deep learning algorithms with the intrinsic features of CNN-RNN to stream the fetal heart rate abnormalities in real-time patients enabling better efficiency than prior reported findings.

The key flaw of the prior methods is that they solely performed fragmentation of the fetal's heart chamber and blood vessel rather than an extensive prenatal FHD diagnosis. Moreover, the embryo's heart petite scale and imprecise anatomical features render it more difficult to prognose 4CV and 3VS in the fetal heart. Furthermore, several cardiac extraction methods are inappropriate since the congenital heart constantly changes in every

constraint. Despite this, most CNN and RNN acquire fetal features from the overall image where image-leveling of the heart region, occlusion and clutter complicates to precisely prognose the four-chamber and blood vessels.

In summary, our key contributions are outlined as follows: The research endeavours the defects septation of the cardiac chambers and blood vessels to retrieve congenital cardiac malformations. Based on current research developments of several DL and meta-heuristic algorithms, the intent work aims to examine the internal functioning of the fetus's heart in ultrasound imaging via two unique methods.

1. The first leverages a novel CNN of VGG 16 with the augmented wiener filter and multi-level ROI framework to characterize the fetal diseased chamber.
2. Succeeding, the second assesses the 3-vessel blood flow amongst fetal cardiac abnormalities via DRNN utilizing Median Modified Wiener Filter (MMWF) with region-based segmentation. The acquired model resulted in high precision on the FHD testimony.

The Structure of the paper is listed below:

Section 2 depicts the proposed methodology and the acquisition of the research. The results of the proposed VGG16 and DRNN are discussed in section 3. Section 4 summarizes the performance and training phase of the proposed model. The significance of the study is concluded in section 5.

2. Proposed Methodology

The prominent methodology in Figure 2 exploits the key fragment of this research to detect the septal flaw at all phases as follows:

1. Pre-configured regions that use distinct image forms are set up as established resolutions for de-noising and enhancement.
2. Segmentation masks with high boundary specialization are defined to generate regional proposals for cases of septal defects if positive.
3. In subsequent, composite featured regions are pruned using non-maximum suppressed classification and determine the presence or absence of abnormalities in the septum, i.e., ASDs, VSDs, and AVSDs.

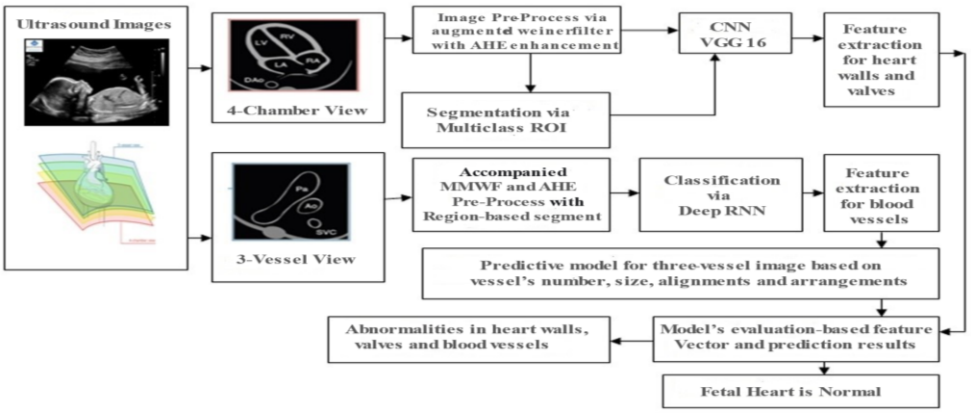

Figure 2. Overall proposed methodology for FHD.

2.1. Ultrasound Fetal Heart Image Acquisition

Table 1 depicts the prenatal fetal cardiac ultrasound datasets accessed through the Digital Imaging and Communications in Medicine (DICOM) from Mohammad Hoesin Medical University's associated Hospital in Indonesia via the radiopaedia web [35] with the patient's confidentiality of both normal and abnormal fetal heart planes. The data was gathered and reviewed by trained sonographers using Ganglionic Eminence (GE), Mindray, Philips, and subsequent ultrasonic devices after the patient had been notified. Figure 3 depicts the fetal cardiac screening via sonographic scanning planes. The size of the collected data includes 1527 images in total from pregnant women who have been testified between 18 to 22 weeks of gestation with testified 4-chamber (RV, RA, LV, LA) and 3-vessel (SVC, PA, AO) scan rate of 465, 326 normal and 326, 409 abnormal images which guarantee the accurate result analysis.

Table 1. FHD dataset acquirement.

S. No	Image planes	Normal images	Anomalous images	Total images
1.	4CS	465	326	791
2.	3VS	326	409	735
3.	Total image planes	791	735	1527

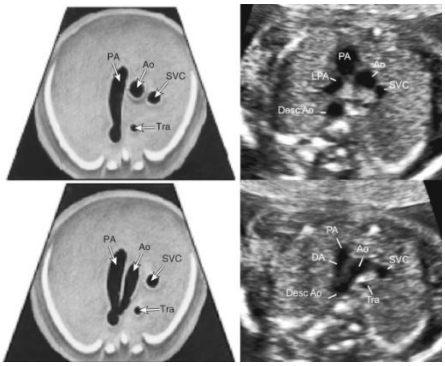

Figure 3. Sonographic scanning planes for fetal cardiac screening.

2.2. Phase of Ultrasound Image Pre-Processing

Ultrasound screening has been the forefront and conventional testing method to prognose atherosclerosis. To accurately identify carotid plaque, the afflicted region of the carotid artery ought to be segregated from the ultrasonic image because noise originates during the capture of arterial images resulting from the high-frequency rate which reflects the state of the data entering the sensors. Several methods are being developed to detect the plaque in ultrasonic data. Herein, the image processing and restorations are crucial procedures for obtaining de-noised enhanced images [24, 40]. The preliminary processing is the initial stage where the nature of the noises i.e., Speckle and Gaussian noise are identified and diminished via the AWF and MMWF de-noising algorithms integrated with the Adaptive Histogram Equalization (AHE) strategy to obtain the fetal image of excellent quality. This combined approach eliminates and filters out multiplicative noises with improved fetal image acquisition.

2.2.1. Wiener Filter Augmentation

The input fetal acquisition images were fed into the Augmented Wiener Filter (AWF) [20] to acquire the noise-prone deteriorated images in the non-linear temporal region using the appropriately stated numerical Equations (1) and (2):

$$g(x,y) = f(x,y) * u(x,y) + n(x,y) \quad (1)$$

$$h(x,y) = R[g(x,y)] \quad (2)$$

where $f(x, y)$ is the assimilated image, $u(x, y)$ is the image degraded function, * represents convolution, $n(x, y)$ showcases the noise disturbances i.e., Speckle and Gaussian noise [27], $g(x, y)$ is the deteriorated image, and $h(x, y)$ enumerates the resultant image via Redistribution (R).

A masking matrix of size n x m is created initially via the spatial noise [18] elimination filter which is then utilized to compute the new pixel for the downgraded image concerning pixel size and value. Utmost, every pixel value is transposed by the average filter [15] of the mean pixel corresponding to the masking matrix at the centred pixel value. The AWF includes both the variation and median values of pixels in the n, m dimensions as enumerated in Equations (3) and (4). As a result, the misfits can be eliminated without affecting image clarity.

$$\mu = \frac{1}{NM} \sum_{n,m\epsilon\eta} a(n,m) \quad (3)$$

$$\sigma^2 = \frac{1}{NM} \sum_{n,m\epsilon\eta} a^2(n,m) - \mu^2 \quad (4)$$

where μ is the mean, σ^2 represents the Gaussian noise variance in the image and n, m enumerates the mask matrix pixel size of regional dimensions h. The AWF is fitted to the additional pixels equated as $b_w(n,m)$ employing the estimated metrices in Equation (5).

$$b_w(n,m) = \mu + \frac{(\sigma^2 - v^2)}{\sigma^2} . (a(n,m) - \mu) \quad (5)$$

Where v^2 is the noise dispersion of the mask metrics. Aside from the de-noising, AWF estimates to replicate biometric parameters generated from the segmented region, which are clinically evaluated for the fetal heart to achieve highly categorized prognosis results.

2.2.2. Median Modified Wiener Filter (MMWF) De-Noising Enhancement

The reflection fronts of ultrasound waves cause random speckle noise in the acquired fetal images. The existence of noise with speckles degrades the image quality and obscures image features, affecting segmentation, feature classification and most significantly disease detection. The standardisation of metrics taken from fetal ultrasound scans will aid physicians in making accurate diagnoses. Cannistraci *et al*. [9] and Cannistraci *et al*. [10] developed the MMWF approach to minimize noise dispersion in deteriorated images. This MMWF is used to denoise the surrounding region of blurred pixels and enhance its quality via adaptive histogram equalization [1, 43]. Relying on the wiener filter, the MMWF approach largely diminishes the interior and exterior noise signal. The MMWF masks the dimensions and pixel counts, reducing chaos in the deteriorated image. The median ($\tilde{\mu}$) value replaces the mean value (μ) in the wiener filter calculation. MMWF is formatted in Equation (6) as follows:

$$b_{mnwf}(n,m) = \tilde{\mu} + \frac{(\sigma^2 - v^2)}{\sigma^2} (a(n,m) - \tilde{\mu}) \quad (6)$$

The MMWF technique benefits in improving the image quality of degraded images where the edge signal is retained from the drop-off effect as correlated and outperforms traditional filters in terms of denoising effect and boarding the contour signal while removing the neighboring noise signals as enumerated in Figure 4.

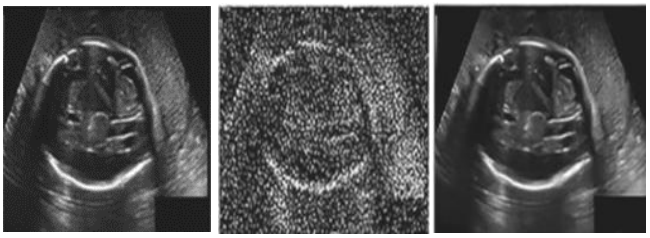

a) Original Image. b) Image with speckle noise. c) De-noised MMWF image.

Figure 4. Instance of MMWF de-noised fetal image.

2.2.3. Evaluation of Image Qualities

Equations (7), (8), and (9) determine the Signal-to-Noise Ratio (SNR) [21], COVariance (COV) [28], and Contrast-to-Noise Ratio (CNR) [37] deliberately to assess the phantom images generated by MMWF noise reduction filters.

$$SNR = \frac{S_A}{\sigma_A} \tag{7}$$

$$COV = \frac{\sigma_A}{S_A} \tag{8}$$

$$CNR = \frac{|S_A - S_B|}{\sqrt{\sigma_A^2 + \sigma_B^2}} \tag{9}$$

Where S_A and σ_A are the mean and variance computation for Region Of Interest (ROI), S_B and σ_B determines the mean and standard deviations of the surrounded noise for ROI.

Although a proper selection of de-noised threshold values may eventually disrupt false regions, there exists undesired information that needs to be segmented from the images. For this, the segmentation algorithm must be applied after the pre-process.

2.3. Segmentation Phase

Following the most current referendum [38], segmentation on region-based generates fetal characteristics with an immediate level set. Thus, this study applied a unique and prominent image segmentation algorithm-ROI with the highest entropy to segment and identify the tumor region in the bounding regression by assessing defect size. The segmentation task first computes the pre-processed fetal data, i.e., the histogram value of the grey-scale fetal image, and then masks it with ground truth. Feature maps are labeled to produce segmented fetal features with the regression region to separate the foreground image (i.e., diseased area) from the background in the four-chamber and 3-vessel region, as shown in Figure 5.

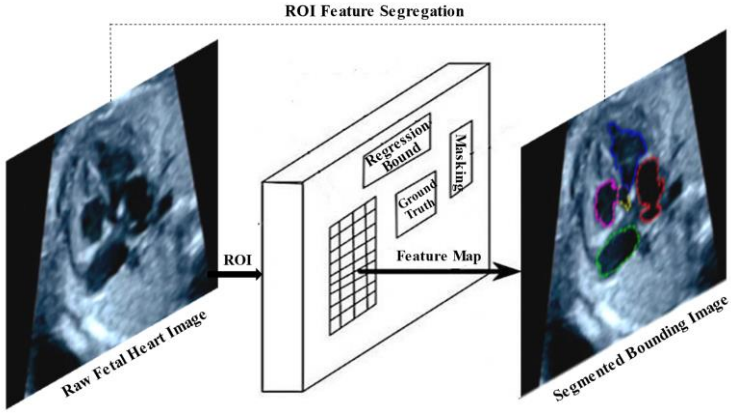

Figure 5. Segmented ROI fetal heart image.

2.4. Convolutional Neural Network (CNN) Integrated VGG-16

The deep-learning neural network CNN is the forefront design in current sectors to recognize patterns of structured arrays with high-yielding rates and numerous throughput transitions resulting in radial breakthroughs in the inflating learning fields.

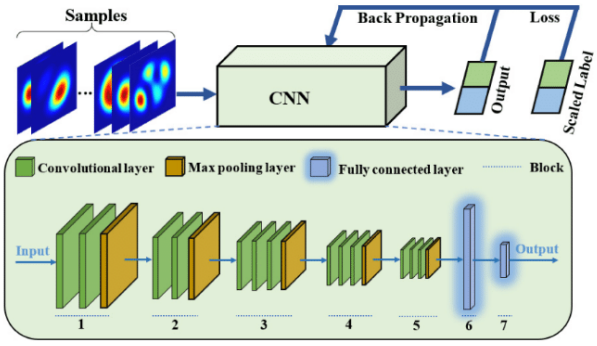

Figure 6. CNN architectural design.

The classification task is accomplished by modifying the CNN via the VGG Net, which primarily boosts the precision in the imaging design phase [3] with the network outputs and inputs. The proposed model has a grey beam appearance with the filter area layer of the VGG model by 3 3 3 to 3 3 1 dimensions. As enumerated in Figure 6, the propounded CNN layout is detached into seven blocks where the first set of five blocks are stepped into a couple of layering convolutions, maximum pooling and in subsequent with fully-connected and softmax. The Convolutional Layer (CL), which is similar to the filter is a significant part of Neural Networks (NN) as wholesome convolutional kernels. The size of CL is determined by the network dimensions of 3×3, 5×5, 7×7, and 11×11 with the fluctuated activation function and pooling layer. The augmented input image is subjected to a weighted mean-based computation i.e., backpropagation on the convolution kernel's setup size with the outcome of the image as a conclusion matrix. This phase determines the duration of each convolutional kernel move, and end convolution value through multiplying the convolution kernel variables with the resultant pixel values in the matrix. The total amount of image features that are extracted during the convolution process differs based on the step size, convolution kernel size, and settings where the size of the entire image featured matrix will be decreased through the estimation of kernel shift. Next, a labeled stimulation-activation function modulates the samples in an increasing monotonic style, mitigating CL's

determinate responses. The attenuated output samples from the interim activation is received by the max pooling layer, reducing the spatial dimensions of the feature maps. The acquired result undergoes transmission via a Fully Connected Neural Network (FCNN) incorporating softmax, which generates the final class anticipation and classifies the resultant image. Utilizing the propounded model, image classification challenges with distinct existing models via comprehension of deep learning in computer vision.

2.4.1. VGG 16 Architectural Design for Fetal Detection

Figure 7 shows the architectural design of VGG 16 Net that upholds 92.7% top-5 trial precision at the ImageNet datasets and in holds 14 million snaps from 1000 groups. The ImageNet dataset's trial is to include images with a defined enormity of 224x224 and RGB passages. As a result, inputs are given as tensors of (224, 224, 3) and generate 1000 vectors.

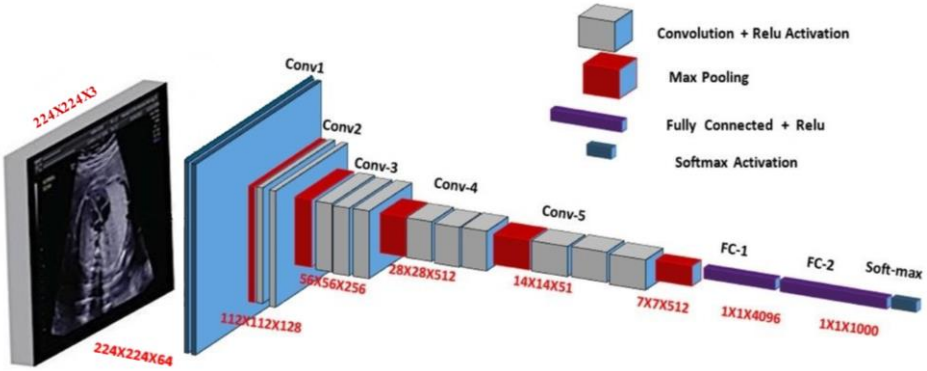

Figure 7. Integrated VGG-16 architecture.

VGG 16 reflects the likelihood of classification for the given class via probability vector $\hat{y}$. For instance, the model provides forecast images which relates to class 0 with probability 1, class 1 escorted by probability 0.05, class 2 escorted by probability 0.05, class 3 over 0.03, class 780 with 0.72, class 999 with probability 0.05, and all other subsequent classes over 0. In conclusion, the categorization paves the path via FCNN and softmax value to guarantee the total probabilities as escalated in Equation (10).

$$\hat{y} = \begin{bmatrix} \widehat{y0} \\ \widehat{y1} \\ \widehat{y2} \\ \widehat{y3} \\ . \\ . \\ . \\ \widehat{y999} \end{bmatrix} \quad \hat{y} = \begin{bmatrix} \widehat{y0} = 0.1 \\ 0.05 \\ 0.05 \\ 0.03 \\ . \\ . \\ . \\ \hat{y}780 = 0.72 \\ . \\ . \\ \hat{y}999 = 0.05 \end{bmatrix} \tag{10}$$

2.4.2. VGG 16 Intern Filter Design and Object Localization in Image

To carry out the localization prognosis, the class score is displaced by the boundary traits contention values where a 4-D vector with centre dimensions (x, y), height, and width is determined. VGG 16 localizing design comes in two distinct forms:

1. Global boundaries (resulting in four feature vectors).
2. Class-specific boundaries (resulting in a four-parameter vector).

The research tested both methods on the VGG 16 design where in case switches from classifying loss to regress loss problems, which penetrates the departure of anticipated loss from the real world.

The VGG Net 16 is stimulated with an input image size of (224, 224, 3) wherein the first two levels claim 64 channels with similar width and filter size of 3x3. Next, a max pool layer with a stride of (2, 2), two layers of CONVolution (conv) phasing with 128 and (3, 3) filtration size (3, 3) is implemented. In subsequent, the second phase of the convolution filter estimates (3, 3) widths and 256 filtrations whereas the third phase enumerates 2-layer conv of 512 filters with identical size (3, 3) and spacing. In last, a 3-layer conv of 51 filter size frames the residual block. The resultant image traits (7, 7, 512) feature map via convolution stack and max pool. To avoid changes in the image's spatial characteristics, 1-pixel padding is included after each layer of convolution. After the residual blocks of convolution, two consecutive FCNN linked Relu layers take the final feature vector as input and generate (1, 4096) vectors as output and the final softmax layer outcomes 1000 channels for classifying the classes.

2.5. Deep Recurrent Neural Network Enframement

The propounded 3-vessel view detection put forth an enhanced DRNN model [14], a forefront DL which incorporate output from prior input of current phase. The inputs and outputs of DRNN are sequentially independent, but when predicting the next scenario, the current work is needed, where it upholds the previous

steps. The DRNN was created to detect and solve the fetal dilemma using the hidden Layer. In DRNNs, the Hidden state is the crucial feature that retains information about the image sequence i.e., Memory State. Similar to CNN, DRNN handles from input to output. Further, it employs feedback loop, such as backpropagation via time and loop the input back into the network during the computing process. This links input, allowing DRNNs to handle image's sequential and temporal data. The diminished backpropagation via time DRNN scenes the number of time steps in the input sequence which has been limited by a truncation. This benefits deep recurrent neural networks in sequence-to-image models i.e., the input sequence to output image.

2.5.1. Architecture Design of DRNN

Figure 8 illustrates the DRNN internal design of input (X_t) and output (L_t) with a similar weight matrix (w) across the network and computed hidden state (h_t) as determined in the recursive Equation (11)

$$h=\sigma(UX + W_{h-1} + L) \tag{11}$$

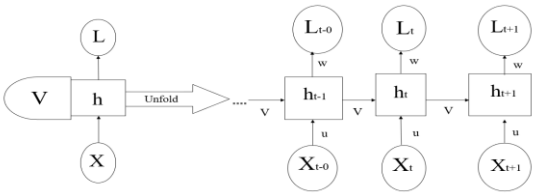

Figure 8. Architectural design block of deep recurrent neural network.

Where h is the hidden state, σ is the numerical variable to modify input features, U represents the unfold regression of Neural Network (NN), X is the input feature, W estimates the weight matrix and L is the output threshold.

The DRNN Process is analyzed using linear regression (v) where the continuous output value is predicted using the regression algorithm to determine whether input features and output values are linearly related. Succeeding with the input sequences (X) and linked labels (L), the model trains over 100 epochs and optimizes the model parameters to minimize categorical cross-entropy loss. In eventual, the weighted sum of input features predicts the output value.

2.6. DRNN feature Extraction for 3-Vessel PA, AO and SVC Via Region-based LPB and HOG

Feature extraction, which involves proceeding detectors of every image is the initial step in creating a bag of visual knowledge regarding the statistical data where a grid is applied at regular intervals to extract several type of local unaffected descriptor and extract mean RGB values from random locations in the images. Figure 9 estimates the texture feature extraction methods of 3-vessel view where the variance is calculated based on the combination of features- Local Binary Pattern (LBP) and Histogram of Oriented Gradient (HOG) [53] to perform distinct fetal images via histogram equalization process.

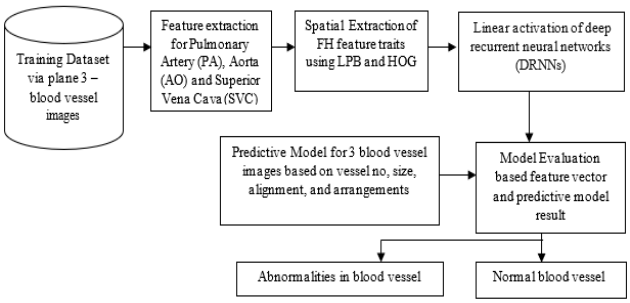

Figure 9. Blood vessel extraction using DRNN.

2.6.1. Extraction of Texture Features for Multi-Level Segment Zone of Interests

In the propounded model, the forefront region and texture-enumerated LPB approach is implemented to regulate and extract texture characteristics with rotational and grey scale consistency where the centered pixels serves as threshold for the initial LBP operator, which is specified in the nxm neighborhood pixels as core component and adjacent matrix. The primary LBP technique imputes to expand the spatial operation range upto 20x20 dimensions as represented in Equation (12) and the calculation for the core and its surrounding pixels is estimated in Equation (13).

LBP's precise calculation is as follows:

$$LBP_{(s_c,y_c)} = \sum_{i=0}^{i=\delta} s(g_p - g_c)\, 2^i \tag{12}$$

$$s(g_p - g_c) = \begin{cases} 1, \{g_p - g_c\} \geq 0 \\ 0, \{g_p - g_c\} < 0 \end{cases} \tag{13}$$

Where P represents central pixel (XC, YC), g_c is the grayscale value of the central pixels, g_p is the greyscale value of neighborhood pixels.

Next in Current, HOG makes up more significant function for extracting texture features within the realm of machine vision wherein grayscale and segregated image processing has been evinced, particularly in the areas of object tracking and detection. The idea behind the path of the gradient histogram is to employ gradient operations [−1 0 1] and [−1 0 1] for every central pixel and to acquire the gradient's direction and amplitude of every pixel. The magnitude and direction of the gradient are determined by Equations (14) and (15).

$$\begin{cases} I_x = F(x+1, y) - F(x-1, y) \\ I_y = F(x, y+1) - F(x, y-1) \end{cases} \tag{14}$$

$$m(x,y) = \sqrt{I_x^2 + I_y^2} \tag{15}$$

$$\theta(x,y) = \tan^{-1}\frac{y}{I^x} \in [0{,}360°) or \in [0{,}180°) \tag{16}$$

Where F is the feature extraction, (x, y) enumerates the magnitude gradient of spatial dimensions, l_x^2 and l_y^2 are

the gradients directional bitmap.

In order to gain access to the histogram representation of each cell, the target image is portioned based on cell size during the texture feature extraction stage and then restructure the HOG and LBP extracted features into several neighboring cell arrays. Equation (16) derives the structural distributions and gradients directional bitmap on the fetal image combined with the histogram parameters to generate the output features i.e., computation of each cell's binary pattern and the gradient histogram with similar cell size and non-overlap in distinct location data as displayed in Figure 10. So that the image depicts as the sphere of pixels in matrix structures or vectors and can be estimation of manifestation of Bag Of Features (BOF) [58]. BOF code to traits in accelerated and stabilized attribute vectors for automatic feature segmentation and predicts the model for vessel images with determined number, size, equilibrium, and vessel configurations as depicted in Figure 11. Thus retrieves the LPB and HOG model to perform high in distinguishing aberrant and normal fetal heart planes in optimal regions for the identification of hereditary heart defects.

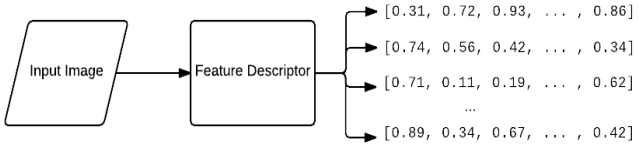

Figure 10. LPB and HOG computation of feature vector arrangement.

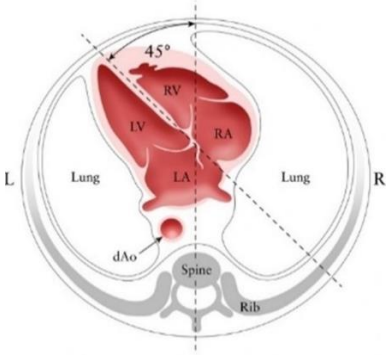

Figure 11. BOF extraction model of fetal heart using multiple feature vectors.

3. Results and Discussions

3.1. Four-Chamber Detection via Integrated CNN

The proposed work is carried out using MATLAB R2023a software and the dataset results are acquired from the retrospective research data examined at Mohammad Hoesin Healthcare in Indonesia and the Radiopaedia site via Digital Imaging and Communications in Medicine (DICOM). In ideal, Figure 12 depicts the input image of the second-trimester fetal ultrasound 4C scan view.

Figure 12. Fetal ultrasonography-input image.

3.2. AWF De-Noising and AHE Image Enhancement

In commencing with the de-noising phase, Figure 13 delineates the outcome of the preliminary processing via the wiener filter augmentation procedure. The AWF image showcased speckle noise being identified and diminished with improved feature intensity from the simulated dataset.

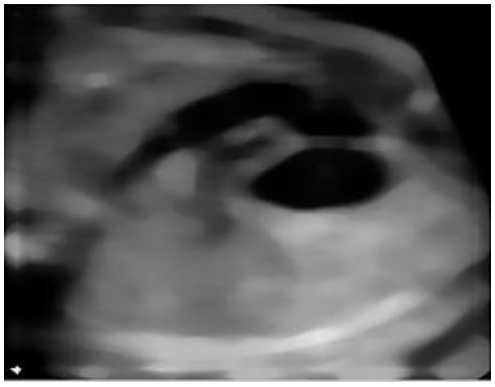

Figure 13. Augmented wiener filtered image.

Succeeding, the collation of the input and de-noised filtering with stretched contrast imagery (i.e., the normalisation) alters the variation of image value with respect to noise intensity as depicted in Figures 14 and 15. This preliminary phase in Figure 15 results with the deployed Local Gaussian-Markov Random Field (LG-MRF) in characterising the image's regional traits and hyperparameter in replenishing spatial correlation between adjacent pixel intensities.

Figure 14. Comparison of input and AWF image.

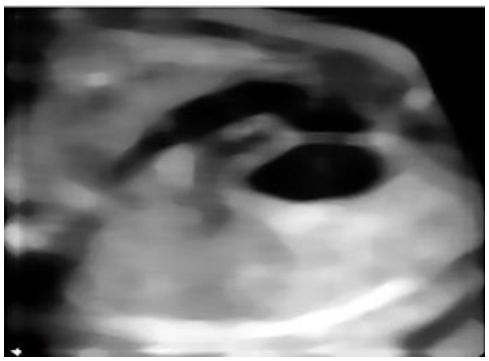

Figure 15. Contrast stretched image.

Figures 16 and 17 illustrate the Adaptive Histogram Equalization (AHE) output and its value plot graph representation. AHE hikes the peak value of the histogram pixels along the y-axis and the image's size along the x-axis and maps the image trait's functional slope. AHE fabricates the minimal input intensity values to conceive a wide range of output intensity values which then conceptualized as a redistribution of the clipped pixels to augment the image enhancement.

Figure 16. AHE Image view.

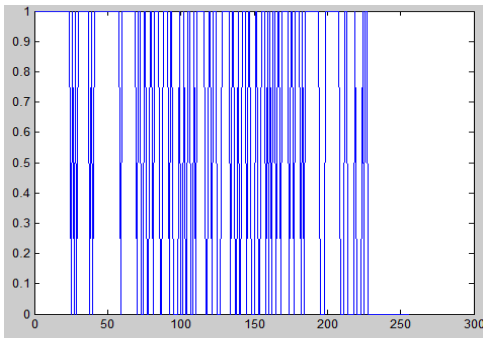

Figure 17. Graphical view of AHE value plot.

3.2.1. Multi-Level ROI Image Segmentation

Figure 18 renders the segmentation labeling via ground truth detection of four-chamber fetal imagery segregated to ROI. The ROI section depicted in Figures 19 and 20 includes vital featured data using the threshold determination of the adaptable histogram exploiting the multilevel segmented region. From the segmented image, the prediction model VGG 16 algorithm retrieve the traits of the diseased feature region of fetal heart anatomy which estimates more comprehensive depiction of septal defects composition as exploited in Figure 21.

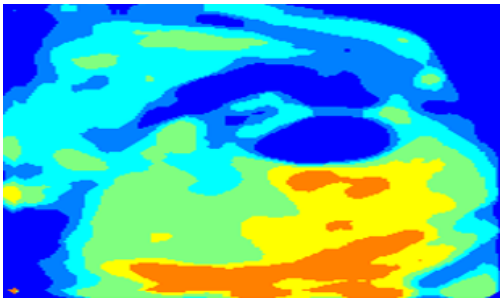

Figure 18. Multi-level ROI segmentation.

Figure 19. Fetal heart region's segmented output.

Figure 20. Segmented output phase based on predictive modelling.

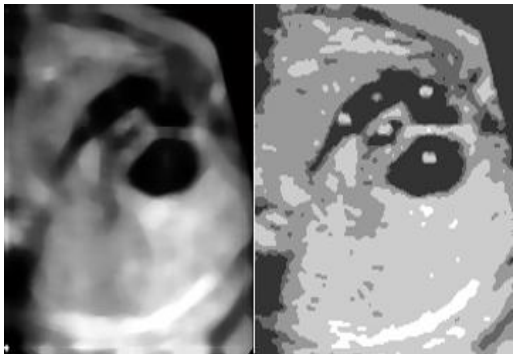

Figure 21. FHD prediction model output.

3.2.2. Image Classification via CNN Integrated VGG 16 Net

Succeeding with the final phase of the segregated image, Figure 22 pictures the detection output which estimates the adequate variables that the model is designed to predict. The classification outcome of the CNN beneath different echo intensity levels in the proximal and distal quadriceps stages where the mid-region has the least intensity, most likely caused due to the upsurge in

filament lessons adjacent to the tendon ends and myotendinous juncture.

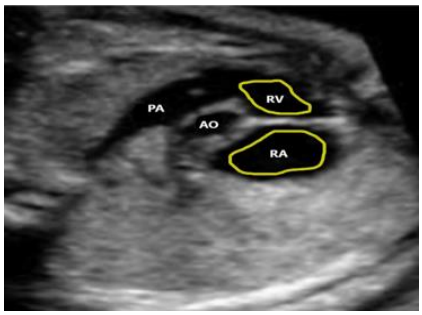

Figure 22. Fetal heart diseases detected image via bounding.

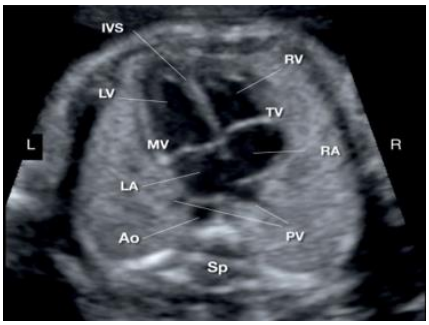

Figure 23. Normal ultrasound fetal image.

The anomalous image in Figure 22 depicts the irregularities on Right Artery (RA) and Right Ventricle (RV) via yellow circular bounding, resulting from the abnormal spiral of the truncus arteriosus and a formation lack of the membranous septum of the fetal anatomy. The heart's walls and components i.e., RA and RV are shaped and matured in irregular disparities via integrated VGG 16 Net accounting for congenital heart defects. Figure 23 showcases the normal fetal imaging of cardiac disorders.

Figure 24 delineates the propounded system's interpreted outputs with accuracy, training, testing and validation set. The graphical measurements are typically plotted with a combined training and validation loss plots in order to analyze their proficiency over time. The degree of accuracy ranges at 99.89%. Both the training and validation accuracy improved and loss ratio diminished at each epoch phase via the network's equivalent operation. The CNN's VGG 16 Net measures the performance of train and test data via the train-test loss. For instance, the iteration error is evaluated on the model's set i.e., subset of the data primitively generated to degrade error of the system. Subsequent error in the training set is added to calculate the training loss alongside test and validation. In addition, utmost each adequate batch is calculated for overall loss curves. Eventually, the integrated VGG-16 is acquired with a classified error of 6.66% and a correlation rate of 25.32%.

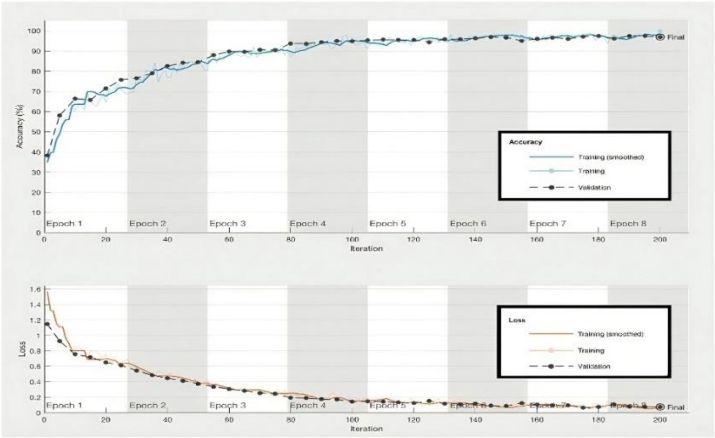

Figure 24. CNN incorporated VGG-16 Net model validation.

3.3. Blood Vessel Detection Via DRNN

Major arteries such as the AOrta (AO), Pulmonary Artery (PA) and Superior Vena Cava (SVC) are transposed in the outflow view of Figure 25, originating from the 3-vessel view.

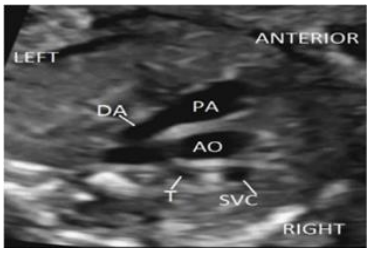

Figure 25. Input blood vessel image.

3.3.1. Enumeration of Preliminary and Segmentation Phase Via MMWF Integrated Region-Based Selection

Figures 25 and 26 illustrate the 3-vessel input imagery with improved filtering outcome utilizing the centered MMWF where the image is de-noised to its intensity level and appropriated for sub-ranged images with differentiated pixel intensity and background. Plus, the average discrepancies resulting from higher intensity is reduced with the optimum threshold. To justify the MMWF process, Figure 27 generates the comparison result via input vs filtered blood vessel image. Ensuing with pre-processed image, Figures 28 and 29 depict the image improvement process utilizing the contrast stretch

AHE and flexible thresholding of groundtruth labeling via masking using region-based segmentation.

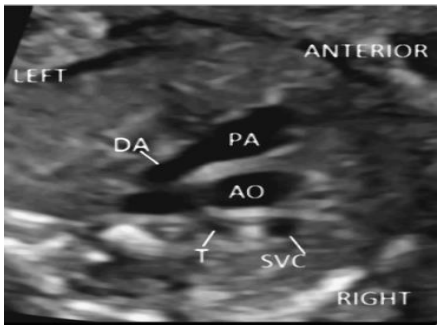

Figure 26. MMWF de-noised image.

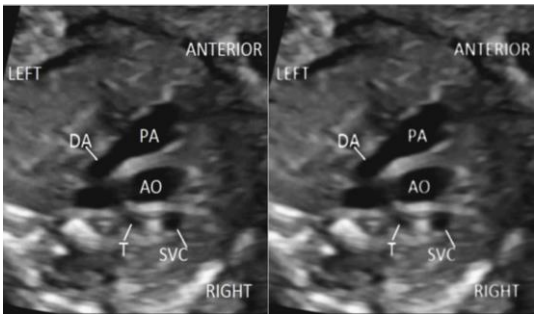

Figure 27. Collation image of input and de-noised vessel view.

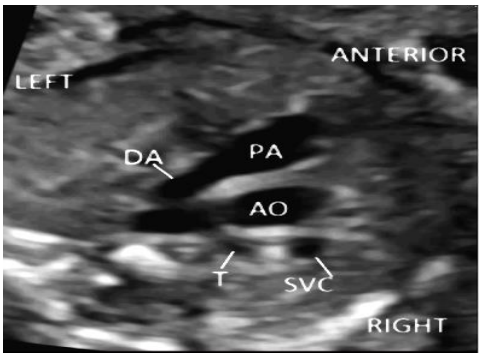

Figure 28. Image enhancement via AHE.

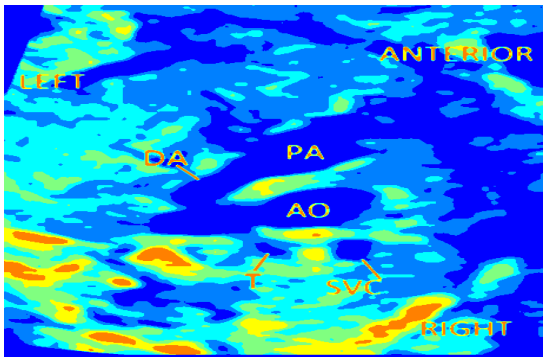

Figure 29. Segmented image via region-based LPB and HOG.

3.3.2. DRNN's 3-Vessel View Fuzzy Detection

In enumeration with region-based, Figure 30 pictures the fabricated outputs of the segmentation phase paired with the dark blue region of the fetal cardiac ultrasound images of the PA, AO, and SVC using LPB and HOG which necessitated the appropriate feature extraction and segregated the foreground and background areas from the pre-processed region. Enclosing, the segmented region is trained via classifcation wherein Figure 31 displays the detection output of DRNN training model with the predictive yellow bounding mask in the diseased PA and AO region with image precision acquirement of 98.7%. The division of the classified area detection has resembled as inconsistent criteria i.e., ischemia regions. The fetus's ischemia area of the interior and exterior has been covered and characterised via segregated region-based segments and DRNN.

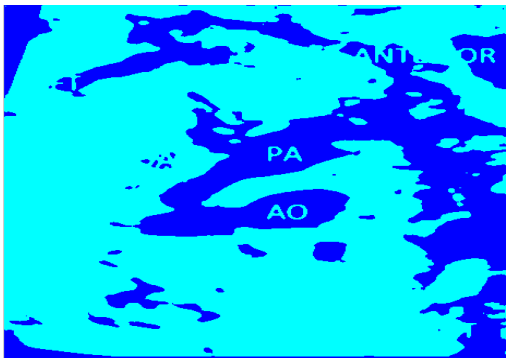

Figure 30. Predictive segmented region of blood vessel image.

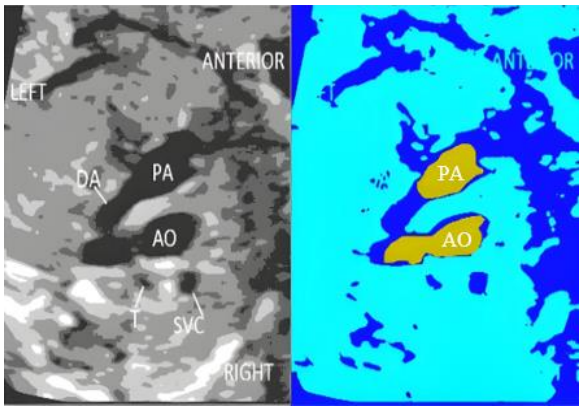

Figure 31. Fetal ischemia detection via DRNN.

4. Performance and Training Phase

The following stage incorporates the statistical and simulated findings of the intended CNN and DRNN in Figures 32 to 35 using the obtained dataset with the efficacy of the parametric assessment which delineates the training phase of the neural network of the specific instance accomplished by calculating the variation among the overall system's processing outcome i.e., the desired predictions. The network then modifies its weight link in accordance with a learning rule and error rate. The automated image classification NN training depicted in Figure 32 utilized the levenberg-marquardt algorithm in driving healthcare systems of NN performance phase and regression plots. Similar to feedforward neural networks, this NN have recurrent connections associated with tap delays and has been implied with finite input response of the Time Delay Net (TDN) and Distributed Delay Net (DDN) that validates the time-series and sequential data.

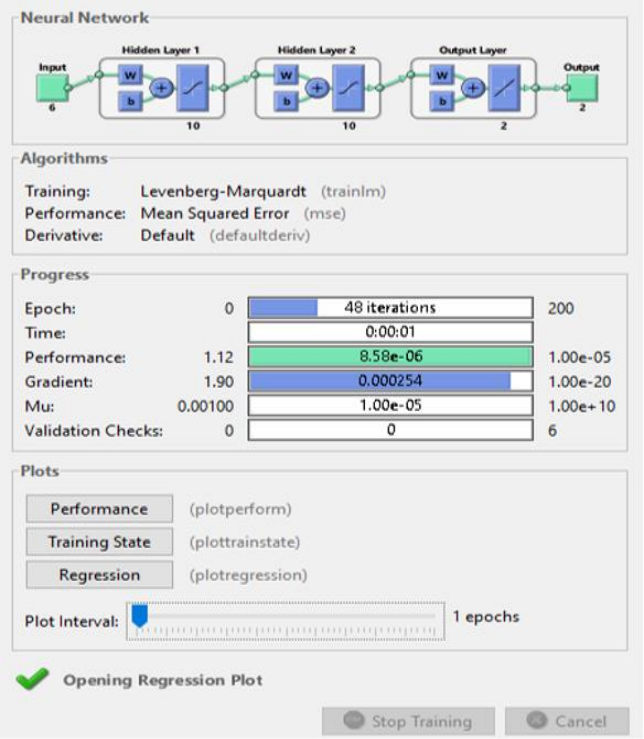

Figure 32. Neural network training.

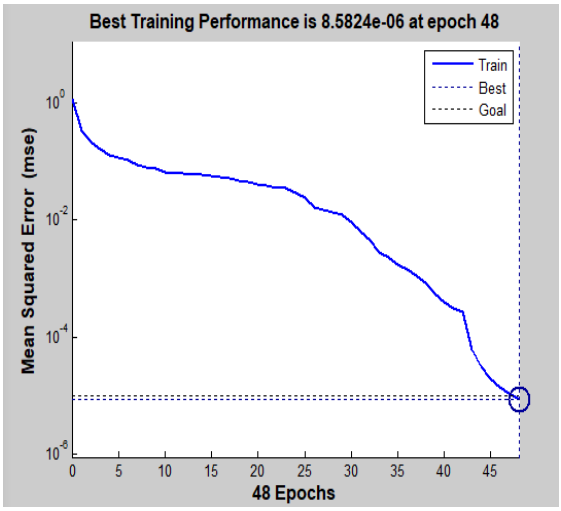

Figure 33. Training performance.

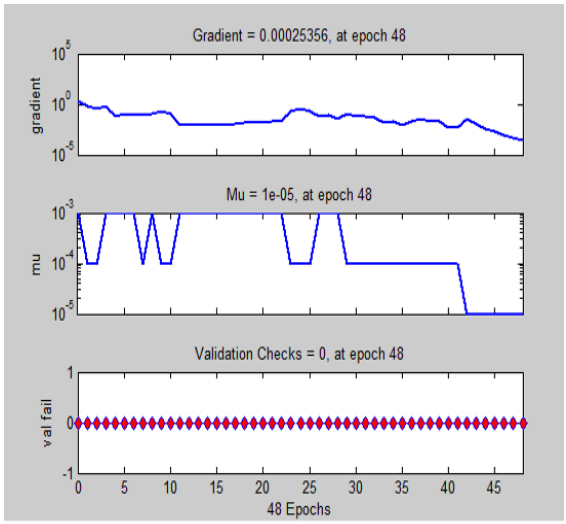

Figure 34. Gradient and epochs.

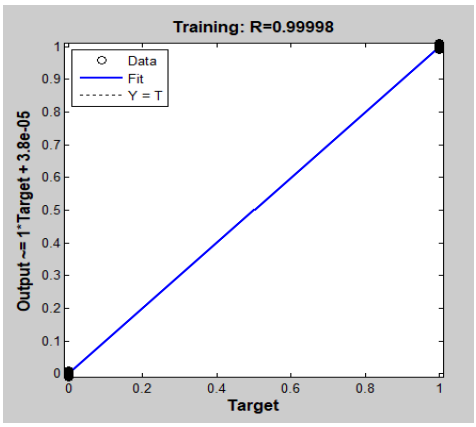

Figure 35. Training regression fit curve.

The performance graph in Figure 33 displays the status of the training state pursuant to the no. of iterations and the Mean Squared Error (MSE) with the succession of 8.5824e-06 network validation efficiency at epoch 48. The commencement and recurrence of errors after epoch 48 show that the data match is ideal in Figure 34, with an overall gradient of 0.00025356, Mu of 1e-05, and zero validation check. The linear graph in Figure 35 represents the target (T) and output (y) dataset in a straight-line equation Y=T with the overall 0.99998 regression R-value for the training data set, which is close to 1 and the trained neural network emerged to be more accurate.

4.1. Model VGG-16 and DRNN's Confusion Metrices

This test yields a 2 by 2 matrix of confusion entries in Equations (17) to (20) for True Positive (TP), True Negative (TN), False Positive (FP), and False Negative (FN) [13] with the widely used evaluation metrics accuracy, sensitivity, specificity, recall and F1-Score rate [46] to estimate the efficiency of the propounded VGG-16 and DRNN models.

In context to FHD, Accuracy escalates the proportion to correctly identify the disease's presence and absence via the propounded VGG 16 and DRNN distinct to the total no. of predictions.

$$Accuracy = \frac{TP + TN}{TP + FP + TN + FN} \quad (17)$$

Sensitivity/Recall enumerates the proportion of actual prediction i.e., true positive FHD cases correctly identified by the proposed model.

$$Sensitivity/Recall = \frac{TP}{TP+FP} \quad (18)$$

Specificity depicts the proportion of actual negative FHD cases i.e., disease absent, correctly identified by the integrated CNN and RNN.

$$Specificity = \frac{TN}{TN + FP} \quad (19)$$

F1-score enumerates the precise proportion of the balanced measure i.e., target and actual FHD test case.

$$F1 - Score = \frac{TP}{TP + 1/2(FP + FN)} \quad (20)$$

Where TP is the test outcome that correctly indicates the FHD with the confirmed presence of the defect, TN pictures the test enumeration that correctly identifies the absence of a fetal heart condition i.e., four-chamber and blood vessels lesion when it is truly absent, FP is the test intent that incorrectly pertains to the presence of fetal heart disease when absent, FN showcases the test sequel that incorrectly indicates the absence of fetal heart disease when it is present.

In examined comparison of Figure 36 with existing MRCNN, DCNN and DGACNN, the proposed system is up to 99.89% and 98.7% more accurate whereas accompanied systems estimated with the efficacy of 97.48%, 95.2%, 96%, 90.43% as depicted in Table 2. In evaluating the system's efficacy, the Error Dispersion (EP) i.e., the average error also concerns where the we have generated the PE distribution of the testing samples to insight the average error into the prediction accuracy. In accordance with EP, the propounded CNN has accomplished less than 2% PE for all practical samples in the 3-mode phase, and the pre-trained DRNN has reached a PE of less than 5% and the associated percentage is computed as the coordinate value. The inclusion of the major overflow tracts and flaws in the four-chamber and three-vessel views during cardiac screening has accurately estimated the detection of CHD.

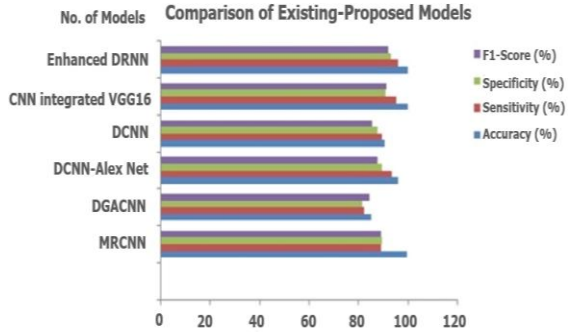

Figure 36. Comparison graph for the existing and proposed system.

Table 2. Performance analysis of existing vs proposed work.

S. No.	System classifier	Model	Accuracy (%)	Sensitivity (%)	Specificity (%)	F1-Score (%)
1.	Existing classifier-I [34]	MRCNN	97.48	92.13	92.21	93.04
2.	Existing classifier-II [33]	DANomaly Wgan-GP and CNN (DGACNN)	95.2	92.2	91.36	94.36
3.	Existing classifier-III [28]	DCNN	96	93.21	94.32	91.42
4.	Existing classifier-IV [29]	DCNN + AlexNet	90.43	89.32	87.65	85.32
5.	Propounded system	Proposed CNN + VGG16	99.89	96.	97.91	96.32
		DRNN	98.7	96	93.3	92

5. Conclusions

Septal defects or FHD are known to be a serious dilemma and have to be anticipated at a premature phase. The deep learning models or algorithms are one with the consequent detection tools utilized for septal defects. The research intended to develop two evident classifier techniques to prognose diseases in four-chamber via CNN incorporated VGG 16 and three-vessel via DRNN of the fetal heart in ultrasound images. Adopting the pre-processing visions of wiener filter augmentation and MMWF techniques, the image quality of acquired fetal images has been assessed with high noise removal and image enhancement. In subsequent, multiclass ROI and region-based segmentation algorithms have designated the pre-processed fetal features of atria, ventricles, pulmonary artery and aorta with masking, grouped the data with ground truth labeling and extracted the diseased features for the further detection procedure of classification. The propounded models CNN and DRNN which rely on MATLAB software have detected the FHD with the inclusive metrics of 99.89% accuracy, 96.2% sensitivity, 97.91% specificity and 96.32% f1-score in four-chamber view and 98.7% accuracy, 96% sensitivity, 93.3% specificity and 92% f1-score in 3-vessel view of the fetal heart with highly estimated comparison of the current cardiac screening detection DL models of MRCNN, DGANN and DCNN. As the outcome of disease abnormalities, FHD parents are counselled at an early stage of their diagnosis.

Declarations

Author contributions: Someshwaran Gunasekaran-Conceptualization, Investigation, Writing-Review, Editing and Resources. Sarada Vivekasaran-Supervision, Validation, Data acquisition, Visualization, and Project administration.

References

[1] Acharya U. and Kumar S., "Genetic Algorithm Based Adaptive Histogram Equalization (GAAHE) Technique for Medical Image Enhancement," *Optik*, vol. 230, pp. 166273, 2021. https://doi.org/10.1016/j.ijleo.2021.166273

[2] Alan M., Aküner M., and Kepez A., "Biosignal Classification and Disease Prediction with Deep Learning," *in Proceedings of the Innovations in Intelligent Systems and Applications Conference*, Istanbul, pp. 1-5, 2020. DOI:10.1109/ASYU50717.2020.9259852

[3] An Y., Li J., Huang L., Leng J., Yang L., and Zhou P., "Deep Learning Enabled Superfast and Accurate M2 Evaluation for Fiber Beams," *Optics Express*, vol. 27, no. 13, pp. 18683-18694, 2019.

https://doi.org/10.1364/OE.27.018683

[4] Asmare M., Woldehanna F., Janssens L., and Vanrumste B., "Rheumatic Heart Disease Detection Using Deep Learning from Spectro-Temporal Representation of Un-Segmented Heart Sounds," *in Proceedings of the 42nd Annual International Conference of the IEEE Engineering in Medicine and Biology Society*, Montreal, pp. 168-171, 2020. DOI:10.1109/EMBC44109.2020.9176544

[5] Babu S., Suneetha A., Babu G., Kumar Y., and Karuna G., "Medical Disease Prediction Using Grey Wolf Optimization and Auto Encoder Based Recurrent Neural Network," *Periodicals of Engineering and Natural Sciences*, vol. 6, no. 1, pp. 229-240, 2018. DOI:10.21533/pen.v6i1.286

[6] Baumgartner C., Kamnitsas K., Matthew J., Fletcher T., Smith S., Koch L., Kainz B., and Rueckert D., "SonoNet: Real-Time Detection and Localisation of Fetal Standard Scan Planes in Freehand Ultrasound," *IEEE Transactions on Medical Imaging*, vol. 36, no. 11, pp. 2204-2215, 2017. DOI:10.1109/TMI.2017.2712367

[7] Bharat R. and Tanveer M., "EEG Signal Classification Using Universum Support Vector Machine,"*Expert Systems with Applications*, vol. 106, pp. 169-182, 2018. https://doi.org/10.1016/j.eswa.2018.03.053

[8] Bridge C., Ioannou C., and Noble J. "Automated Annotation and Quantitative Description of Ultrasound Videos of the Fetal Heart," *Medical Image Analysis*, vol. 36, pp. 147-161, 2017. https://doi.org/10.1016/j.media.2016.11.006

[9] Cannistraci C., Abbas A., and Gao X., "Median Modified Wiener Filter for Nonlinear Adaptive Spatial Denoising of Protein NMR Multidimensional Spectra," *Scientific Reports*, vol. 5, no. 1, pp. 8017, 2015. https://doi.org/10.1038/srep08017

[10] Cannistraci C., Montevecchi F., and Alessio M., "Median-Modified Wiener Filter Provides Efficient Denoising, Preserving Spot Edge and Morphology in 2-DE Image Processing," *Proteomics*, vol. 9, no. 21, pp. 4908-4919, 2009. DOI:10.1002/pmic.200800538

[11] Cheng J., Ni D., Chou Y., Qin J., Tiu C., Chang Y., Huang C., Shen D., and Chen C., "Computer-Aided Diagnosis with Deep Learning Architecture: Applications to Breast Lesions in US Images and Pulmonary Nodules in CT Scans," *Scientific Reports*, vol. 6, no. 1, pp. 24454, 2016. https://doi.org/10.1038/srep24454

[12] Choi E., Schuetz A., Stewart W., and Sun J., "Using Recurrent Neural Network Models for Early Detection of Heart Failure Onset," *Journal of the American Medical Informatics Association*, vol. 24, no. 2, pp. 361-370, 2017. DOI:10.1093/jamia/ocw112

[13] Combs C., Hameed A., Friedman A., Hoskins I., Quality Committee, and Society for Maternal-Fetal Medicine., "Special Statement: Proposed Quality Metrics to Assess Accuracy of Prenatal Detection of Congenital Heart Defects," *American Journal of Obstetrics and Gynecology*, vol. 222, no. 6, pp. 2-9, 2020. https://doi.org/10.1016/j.ajog.2020.02.040

[14] Das S., Mukherjee H., Obaidullah S., Santosh K., Roy K., and Saha C., "Recurrent Neural Network Based Classification of Fetal Heart Rate Using Cardiotocograph," *in Proceedings of the Recent Trends in Image Processing and Pattern Recognition: 2nd International Conference*, Solapur, pp. 226-234, 2019. https://doi.org/10.1007/978-981-13-9184-2_20

[15] De Araujo A., Constantinou C., and Tavares J., "Smoothing of Ultrasound Images Using a New Selective Average Filter," *Expert Systems with Applications*, vol. 60, pp. 96-106, 2016. https://doi.org/10.1016/j.eswa.2016.04.034

[16] Dev M., Nanda N., Maulik D., and Vilchez G., "A Brief History of Fetal Echocardiography and its Impact on the Management of Congenital Heart Disease," *Echocardiography*, vol. 34, no. 12, pp. 1760-1767, 2017. DOI:10.1111/echo.13713

[17] Dong J., Liu S., Liao Y., Wen H., Lei B., Li S., and Wang T., "A Generic Quality Control Framework for Fetal Ultrasound Cardiac Four-Chamber Planes," *IEEE Journal of Biomedical and Health Informatics*, vol. 24, no. 4, pp. 931-942, 2019. DOI:10.1109/JBHI.2019.2948316

[18] Fu H., Zhang A., Sun G., Ren J., Jia X., Pan Z., and Ma H., "A Novel Band Selection and Spatial Noise Reduction Method for Hyperspectral Image Classification," *IEEE Transactions on Geoscience and Remote Sensing*, vol. 60, pp. 1-13, 2022. https://doi.org/10.1109/TGRS.2022.3189015

[19] Gong Y., Zhang Y., Zhu H., Lv J., Cheng Q., Zhang H., He Y., and Wang S., "Fetal Congenital Heart Disease Echocardiogram Screening Based on DGACNN: Adversarial One-Class Classification Combined with Video Transfer Learning," *IEEE Transactions on Medical Imaging*, vol. 39, no. 4, pp. 1206-1222, 2019. DOI:10.1109/TMI.2019.2946059

[20] Gunarathne M., Wansekara W., Wimalarathna G., Godaliyadda G., Ekanayake M., Wijayakulasooriya J., and Rathnayake R., "Fetal Heart Abnormality Detection Based on Subspace Separation and Wiener Filtering," *in Proceedings of the IEEE International Conference on Industrial and Information Systems*, Peradeniya, pp. 1-6, 2017. https://doi.org/10.1109/ICIINFS.2017.8300349

[21] Hasegawa H. and Nagaoka R., "Converting Coherence to Signal-to-Noise Ratio for Enhancement of Adaptive Ultrasound Imaging,"

Ultrasonic Imaging, vol. 42, no. 1, pp. 27-40, 2020. https://doi.org/10.1177/0161734619889384

[22] Leclerc S., Smistad E., Pedrosa J., Ostvik A., Cervenansky F., Espinosa F., Espeland T., Berg E., Jodoin P., and Grenier T., "Deep Learning for Segmentation Using an Open Large-Scale Dataset in 2D Echocardiography," *IEEE transactions on Medical Imaging*, vol. 38, no. 9, pp. 2198-2210, 2019. DOI:10.1109/TMI.2019.2900516

[23] Liu S., Wang Y., Yang X., Lei B., Liu L., Li S., Ni D., and Wang T., "Deep Learning in Medical Ultrasound Analysis: A Review," *Engineering*, vol. 5, no. 2, pp. 261-275, 2019. DOI:10.1016/j.eng.2018.11.020

[24] Lizzi F. and Feleppa E., "Image Processing and Pre-Processing for Medical Ultrasound," *in Proceedings of the 29th Applied Imagery Pattern Recognition Workshop*, Washington, pp. 187-192, 2000. DOI:10.1109/AIPRW.2000.953624

[25] Luo G. and Pan S., "Advances in Interventional Therapy of Fetal Structural Heart Disease," *Journal of Laboratory and Precision Medicine*, vol. 33, no. 6, pp. 555-559, 2018.

[26] Maraci M., Bridge C., Napolitano R., Papageorghiou A., and Noble J., "A Framework for Analysis of Linear Ultrasound Videos to Detect Fetal Presentation and Heartbeat," *Medical Image Analysis*, vol. 37 pp. 22-36, 2017. https://doi.org/10.1016/j.media.2017.01.003

[27] Mehdi M., Tabarestani S., Cabrerizo M., Barreto A., and Adjouadi M., "Denoising of Ultrasound Images Affected by Combined Speckle and Gaussian Noise," *IET Image Processing*, vol. 12, no. 12, pp. 2346-2351, 2018. https://doi.org/10.1049/iet-ipr.2018.5292

[28] Morgan M., Covariance Decomposition of Ultrasonic Backscatter: Application to Estimation-based Image Formation, Ph.D. Thesis, Duke University, 2020. https://hdl.handle.net/10161/20853

[29] Narmadha S., Gokulan S., Pavithra M., Rajmohan R., and Ananthkumar T., "Determination of Various Deep Learning Parameters to Predict Heart Disease for Diabetes Patients," *in Proceedings of the International Conference on System, Computation, Automation and Networking*, Pondicherry, pp. 1-6. 2020. DOI:10.1109/ICSCAN49426.2020.9262317

[30] Nurmaini S., Rachmatullah M., Sapitri A., Darmawahyuni A., Jovandy A., Firdaus F., Tutuko B., and Passarella R., "Accurate Detection of Septal Defects with Fetal Ultrasonography Images Using Deep Learning-Based Multiclass Instance Segmentation," *IEEE Access*, vol. 8, pp. 196160-196174, 2020. DOI:10.1109/ACCESS.2020.3034367

[31] Oktay O., Ferrante E., Kamnitsas K., Heinrich M., Bai W., Caballero J., Cook S., de Marvao A., Dawes T., O'Regan D., "Anatomically Constrained Neural Networks (ACNNs): Application to Cardiac Image Enhancement And Segmentation," *IEEE Transactions on Medical Imaging*, vol. 37, no. 2, pp. 384-395, 2017. DOI:10.1109/TMI.2017.2743464

[32] Pan S., "Exploration and Prospect of Interventional Therapy for Fetal Congenital Heart Diseases in China," *Journal of Interventional Radiology*, vol. 28, no. 10, pp. 915-920, 2019.

[33] Patra A. and Noble J., "Multi-Anatomy Localization in Fetal Echocardiography Videos," *in Proceedings of the IEEE 16th International Symposium on Biomedical Imaging*, Venice, pp. 1761-1764, 2019. DOI:10.1109/ISBI.2019.8759551

[34] Qi X., Zhao B., Guo Y., Lou H., Pan M., Wang B., Peng X., and Chen R., "Quantitative Study of Early Fetal Echocardiography on Normal Fetal Ventricular Diameter and Z-Score," *Chinese Journal of Ultrasonography*, vol. 29, no. 5, pp. 427-433, 2020.

[35] Radiopaedia, https://radiopaedia.org/, Last Visited, 2024.

[36] Richhariya B. and Tanveer M., "Least Squares Projection Twin Support Vector Clustering," *Information Sciences*, vol. 533 pp. 1-23, 2020. https://doi.org/10.1016/j.ins.2020.05.001

[37] Rodriguez-Molares A., Rindal O., D'hooge J., Måsøy S., Austeng A., Bell M., and Torp H., "The Generalized Contrast-to-Noise Ratio: A Formal Definition for Lesion Detectability," *IEEE Transactions on Ultrasonics, Ferroelectrics, and Frequency Control*, vol. 67, no. 4, pp. 745-759, 2019. https://doi.org/10.1109/TUFFC.2019.2956855

[38] Rossi L., Akbar K., and Prati A., "A Novel Region of Interest Extraction Layer for Instance Segmentation," *in Proceedings of the 25th International Conference on Pattern Recognition*, Milan, pp. 2203-2209, 2021. DOI:10.1109/ICPR48806.2021.9412258

[39] Selvathi D. and Chandralekha R., "Fetal Biometric Based Abnormality Detection During Prenatal Development Using Deep Learning Techniques," *Multidimensional Systems and Signal Processing*, vol. 33, no. 1, pp. 1-15, 2022. https://doi.org/10.1007/s11045-021-00765-0

[40] Sharma A. and Singh J., "Image Denoising Using Spatial Domain Filters: A Quantitative Study," *in Proceedings of the 6th International Congress on Image and Signal Processing*, Hangzhou, pp. 293-298, 2013. DOI:10.1109/CISP.2013.6744005

[41] Shi J., Zhou S., Liu X., Zhang Q., Lu M., and Wang T., "Stacked Deep Polynomial Network Based Representation Learning for Tumor Classification with Small Ultrasound Image Dataset," *Neurocomputing*, vol. 194, pp. 87-94,

2016. https://doi.org/10.1016/j.neucom.2016.01.074

[42] Simcha Y., Cohen S., and Messing B., "First and Early Second Trimester Fetal Heart Screening," *Current Opinion in Obstetrics and Gynecology*, vol. 19, no. 2, pp. 177-191, 2007. DOI:10.1097/GCO.0b013e3280895de6

[43] Singh P., Mukundan R., and De Ryke R., "Feature Enhancement in Medical Ultrasound Videos Using Contrast-Limited Adaptive Histogram Equalization," *Journal of Digital Imaging*, vol. 33, no. 1, pp. 273-285, 2020. https://doi.org/10.1007/s10278-019-00211-5

[44] Smistad E. and Løvstakken L., "Vessel Detection in Ultrasound Images Using Deep Convolutional Neural Networks," *in Proceedings of the International Workshop on Deep Learning in Medical Image Analysis*, pp. 30-38, 2016. https://doi.org/10.1007/978-3-319-46976-8_4

[45] Sombune P., Phienphanich P., Phuechpanpaisal S., Muengtaweepongsa S., Ruamthanthong A., and Tantibundhit C., "Automated Embolic Signal Detection Using Deep Convolutional Neural Network," *in Proceedings of the 39th Annual International Conference of the IEEE Engineering in Medicine and Biology Society*, pp. 3365-3368, 2017. DOI:10.1109/EMBC.2017.8037577

[46] Someshwaran G. and Sarada V., "An Improved Detection of Fetal Heart Disease Using Multilayer Perceptron," *in Proceedings of the International Conference on Intelligent Computing for Sustainable Development*, Hyderabad, pp. 186-199, 2023. https://doi.org/10.1007/978-3-031-61298-5_15

[47] Sundaresan V., Bridge C., Ioannou C., and Noble J., "Automated Characterization of the Fetal Heart in Ultrasound Images Using Fully Convolutional Neural Networks," *in Proceedings of the IEEE 14th International Symposium on Biomedical Imaging*, Melbourne, pp. 671-674, 2017. DOI:10.1109/ISBI.2017.7950609

[48] Shinde S. and Martinez-Ovando J., "Heart Disease Detection with Deep Learning Using a Combination of Multiple Input Sources," *in Proceedings of* the *IEEE 5th Ecuador Technical Chapters Meeting*, Cuenca, pp. 1-3, 2021. DOI:10.1109/ETCM53643.2021.9590672

[49] Tanveer M., Gupta T., Shah M., and Richhariya B., "Sparse Twin Support Vector Clustering Using Pinball Loss," *IEEE Journal of Biomedical and Health Informatics*, vol. 25, no. 10, pp. 3776-3783, 2021. DOI:10.1109/JBHI.2021.3059910

[50] Uma R., Roy F., Filly, and Copel J., "Prenatal Imaging: Ultrasonography and Magnetic Resonance Imaging," *Obstetrics and Gynecology*, vol. 112, no. 1, pp. 145, 2008. DOI:10.1097/01.AOG.0000318871.95090.d9

[51] Wang H. and Avillach P., "Diagnostic Classification and Prognostic Prediction Using Common Genetic Variants in Autism Spectrum Disorder: Genotype-Based Deep Learning," *JMIR Medical Informatics*, vol. 9, no. 4, pp. 24754. 2021. https://doi.org/10.2196/24754

[52] Wang H., Li L., Chi L., and Zhao Z., "Autism Screening Using Deep Embedding Representation," *in Proceedings of the 19th International Conference on Computational Science*, Faro, pp. 160-173, 2019. http://dx.doi.org/10.1007/978-3-030-22741-8_12

[53] Wu B., Liu P., Wu H., Liu S., He S., and Lv G., "An Effective Machine-Learning Based Feature Extraction/Recognition Model for Fetal Heart Defect Detection from 2D Ultrasonic Imageries," *CMES-Computer Modeling in Engineering and Sciences*, vol. 134, no. 2, pp. 1069-1089, 2023. DOI:10.32604/cmes.2022.020870

[54] Wu B., Wu H., Du Y., and Liu P., "Automatic Recognition of Fetal Heart Standard Section Based on Fast-RCNN," *in Proceedings of the IEEE 15th International Conference on Anti-Counterfeiting, Security, and Identification*, Xiamen, pp. 70-73, 2021. DOI:10.1109/ASID52932.2021.9651487

[55] Xu L., Liu M., Shen Z., Wang H., Liu X., Wang X., Wang S., Li T., Yu S., and Hou M., "DW-Net: A Cascaded Convolutional Neural Network for Apical Four-Chamber View Segmentation in Fetal Echocardiography," *Computerized Medical Imaging and Graphics*, vol. 80, pp. 101690, 2020. https://doi.org/10.1016/j.compmedimag.2019.101690

[56] Yang L., Ru T., Gu Y., Yang Y., Yang L., and Wang Z., "The Value of Refinement of Four-Chamber Cardiac Screening Technique in Improving Prenatal Diagnosis Rate of Fetal Congenital Heart Disease," *Chinese Journal of Perinatal Medicine*, vol. 17, no. 8, pp. 570-572, 2014.

[57] Yuya H., Muramatsu C., Kobayashi H., Hara T., and Fujita H., "Automated Detection of Masses on Whole Breast Volume Ultrasound Scanner: False Positive Reduction Using Deep Convolutional Neural Network," *in Proceedings of the Conference Record of the Society of Photo-Optical Instrumentation Engineers*, Orlando, pp. 717-722, 2017. https://doi.org/10.1117/12.2254581

[58] Zhang L., Li K., Qi Y., and Wang F., "Local Feature Extracted by the Improved Bag of Features Method for Person Re-Identification," *Neurocomputing*, vol. 458, pp. 690-700, 2021. doi.org/10.1016/j.neucom.2019.12.142

Someshwaran Gunasekaran is currently pursuing his Ph.D in Department of Electronics and Communication Engineering, SRM Institute of Science and Technology, Kattankulathur campus. His research interests include Medical Image Processing, Deep Learning, Computer Vision and VLSI Testing Design.

Sarada Vivekasaran is working as Assistant Professor in Department of Electronics and Communication Engineering, SRM Institute of Science and Technology, Kattankulathur campus. Her research interests include VLSI Low Power Design, Reconfigurable Digital System Design, and VLSI Testing Design.